Dense point cloud acquisition with a low-cost Velodyne VLP-16

Jason Bula[1], Marc-Henri Derron[2], and Gregoire Mariethoz[1]

[1]University of Lausanne, Institute of Earth Surface Dynamics
[1]University of Lausanne, Institute of Earth Sciences

Abstract. This study develops a low-cost terrestrial lidar system (TLS) for dense point cloud acquisition. Our system consists of a VLP-16 lidar scanner produced by Velodyne which we have placed on a motorized rotating platform. This allows to continuously change the direction and densify the scan. Axis correction is performed in post-processing to obtain accurate scans. The system has been compared indoors with a high-cost system, showing an average absolute difference of $\pm$ 2.5 cm. Stability tests demonstrated an average distance of $\pm$ 2 cm between repeated scans with our system. The system has been tested in abandoned mines with promising results. It has a very low price (approximately 4000 dollars) and opens the door to measuring risky sectors where instrument loss is high but information valuable.

1 Introduction

These last decades, remote sensing and associated technologies have been developed and used to greatly improve environmental modelling. In particular, Light Detection and Ranging (hereafter lidar) has been proposed as a tool in geomatics to address such environmental modelling. Lidar technology is based on the Time of Flight (ToF, i.e. the time required by the light emitted by the laser to be reflected and captured again by the system) to measure distances. Lidar is useful for solving many problems. They are therefore widely used in geosciences, in particular for the management and the monitoring of environmental risks such as landslides, rock falls or cavity collapse (Lim et al., 2005 ; Teza et al., 2007 ; Jaboyedoff et al., 2011, Brideau et al., 2012; Royán et al., 2014; Michoud et al., 2015). The reliability of these measuring instruments is well established, but the technology is typically very expensive, which limits the potential applications of such systems.

New lidar-based obstacle avoidance technologies have been under development since the advent of autonomous cars. These mass-produced sensors are cheap but were not initially designed produce dense point clouds, and therefore have reduced ranges and resolutions. These low-cost systems have led to the development of new scanner systems that can be applied for mapping, especially for mobile terrestrial slam-based systems (James and Quinton., 2014 ; Dewez et al., 2017) or UAV slam-based system (Laurent et al,. 2019 ; Li et al,. 2014) and often requires the addition of an inertial station and Global Navigation Satellite System (GNSS).

Instruments used in geodesy such as theodolites or total stations must be calibrated to avoid measurement errors. This principle is also applied to lidar, which is constructed in a similar way. Lidar system calibration is a much studied subject in research. The aim is to determine the parameters that allow systematic errors to be reduced as much as possible. According to Neitzel 2006, three major errors may be present and are respectively : tilting axis error, collimation error, and eccentricity of

the line of sight. Some authors describe up to 21 possible calibration parameters (Lichti., 2007). There are different strategies for calibrating a lidar system. Research proposes a self-calibration based on mathematical models and by making geometric primitives as reference planes (Glennie and Lichti., 2010 ; Lerma and Garcia-San-Miguel 2014) or reference points (Neizel, 2006 ; Kesten et al., 2005). Other authors present calibration methods based on the use of a camera (Amiri Parian and Grün,. 2005 ; Lichti et al,. 2007).

Our study is based on the use of a low-cost lidar system which is the VLP-16 of Velodyne to elaborate of a low-cost TLS. This scanner currently, sold for 4000 dollars, has 16 parallel scan lines in a vertical field of view of ± 15 degrees, and a 360-degree horizontal scan plane (Figure 2c).Our idea was based on the addition of a rotating plate (which is a principle similar to that of many lidar systems) to produce a dense point cloud. Such a system particularly targets applications in rough field conditions, such as for example caves that are difficult to access. In such places there is the likelihood of damage to the equipment due to shocks, water, or dirt, which prevents the use of high-cost equipment. This type of system could also facilitate risk management in mines for the development of cave collapse risk maps, for example. The advantage is that the system is inexpensive, making it particularly suitable for permanent laser scanning in hazardous areas as described in (Williams et al., 2018). In addition, the power consumption of low-cost lidars is often very small, which is suitable for such environments.

The structure of this paper is as follows : section 2 presents the equipment and the constraints associated with it to produce a low-cost system. Section 3 presents the methodology used to produce high-resolution scans. Section 4 presents the result of our system. Section 5 discusses the results and section 6 presents some conclusions.

2   Low-cost hardware

2.1   VLP-16 Lidar

The VLP-16 model has 16 lasers fixed on a rotational head. The main features of the low-cost lidar can be found in table 1.

Table 1. Velodyne VLP-16

Channel	16
Wavelength	903 nm
Ranging accuracy	± 3 cm (Typical)
Measurement Range	Up to 100m
Single Return Data Points	300000 pts/s
Maximum number of returns	2
Field of View (vertical)	30°
Vertical angular resolution	2.0°
Field of View (Horizontal)	360°
Horizontal angular resolution	$0.1° - 0.4°$
Laser rotation	10 Hz
Weight	830 g
Dimension	Ø 103mm, H 72mm
Retail Price	$4000

Each of the 16 parallel scan lines records up to 1875 points every tenth of a second, which corresponds to an angular horizontal resolution of 0.2 ° for a field of view of 360-degrees. Regarding the vertical resolution, the sensor is limited to a field of view of 30 degrees (Figure 2c). The 16 scan lines imply a low vertical angular resolution of 2.0°. Each of the 16 lasers in VLP-16 is individually aimed and, thus, each has a unique set of adjustment parameters. The mathematical model of VLP-16 which calculates the (x,y,z) coordinates is given in (Glennie et Lichti, 2010) as :

$$\begin{bmatrix} x \\ y \\ z \end{bmatrix} = \begin{bmatrix} (s^i * R_i + D_o^i) * cos(\delta_i) * [sin(\varepsilon) * cos(\beta_i) - cos(\varepsilon_i)] - H_o^i * [cos(\varepsilon) * cos(\beta_i) + sin(\varepsilon) * sin(\beta_i)] \\ (s^i * R_i + D_o^i) * cos(\delta_i) * [cos(\varepsilon) * cos(\beta_i) + sin(\varepsilon_i)] + H_o^i * [sin(\varepsilon) * cos(\beta_i) - cos(\varepsilon) * sin(\beta_i)] \\ (s^i * R_i + D_o^i) * sin(\delta_i) + V_o^i \end{bmatrix}$$

Where:

s^i is the distance scale factor for laser i;

50   D_o^i Do is the distance offset for laser i;

δ_i is the vertical rotation correction for laser i;

β_i is the horizontal rotation correction for laser i;

H_o^i is the horizontal offset from scanner frame origin for laser i;

V_o^i is the vertical offset from scanner frame origin for laser i;

55   R_i is the raw distance measurement from laser i;

ε is the encoder angle measurement.

The first six parameters are used to calibrate the system and can be found in the lidar data sheet. R_i and ε come from data collected during a measurement.

Figure 1a shows a photograph of the scanned scene with the same viewing angle, and Figure 1b shows a typical point cloud produced by the VLP-16 with highlighted vertical and horizontal angular resolutions. The poor vertical resolution limits the use of the VLP-16 for terrestrial scanning applications. For example, the low point density makes it difficult to co-register several scans.

2.2 Syrp Genie

With the purpose to have a low-cost design, we select the Syrp Genie Mini (table 2). This motorized head can rotate 360-degrees and sustain the weight of the lidar.

Table 2. Syrp Genie

Max rotation speed	0.58 rpm (35 s for 360-degrees)
Min rotation speed	0.0025 rpm
Payload	4 kg
Hardware Interface	Bluetooth 4.0
Dimensions	91.5 x 91.5 x 46mm
Retail Price	$250
Minimum step	0.005 degree

2.3 Conception and assembly of the custom scanning system

The VLP 16 is mounted on the Syrp Genie Mini, and the entire assembly is set on a photographic tripod and connected to a computer and a power source (Figure 2a). Importantly, the lidar is placed vertically using an L-shaped piece, such that the vertical (low-resolution) and horizontal (high-resolution) directions are now reversed. It is also important to note that the term "vertical" corresponds to the lidar reference system and not necessarily to the direction of the gravitational field. Our goal is to use the slow rotating motion induced by the Syrp Genie Mini to densify the point cloud across the horizontal direction. It includes a stepper motor with a minimum step of 0.005 degree which does not impact the acquisition frequency of the VLP-16. A counterweight is placed on the tripod on the opposite side of the lidar to minimize stresses that can impact the rotation speed and induce an angular distortion.

a)

b)

1) Horizontal angular resolution: 0.1º – 0.4º
2) Vertical angular resolution: 2.0º
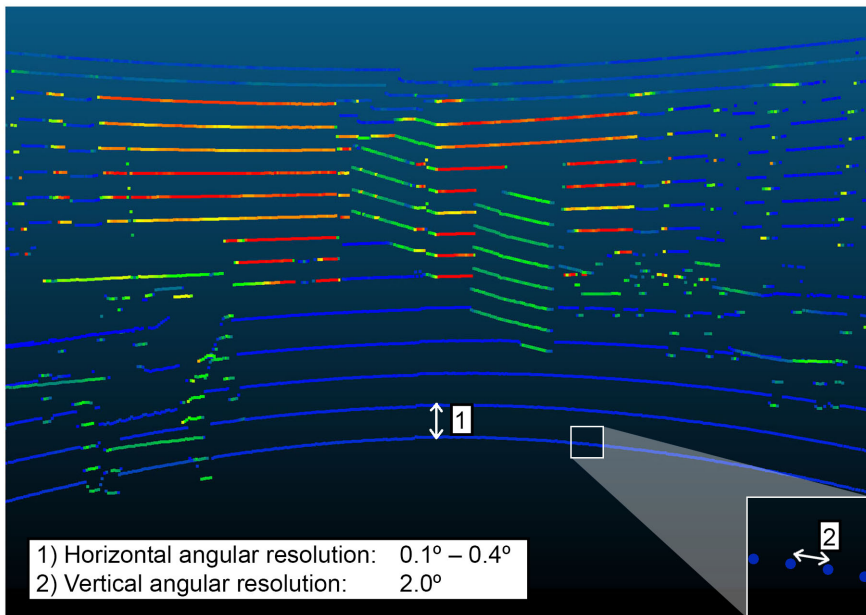
Figure 1. (a) Picture of the scanned scene; (b) a typical scan created with the VLP-16, the color represents the intensity of the returned signal.
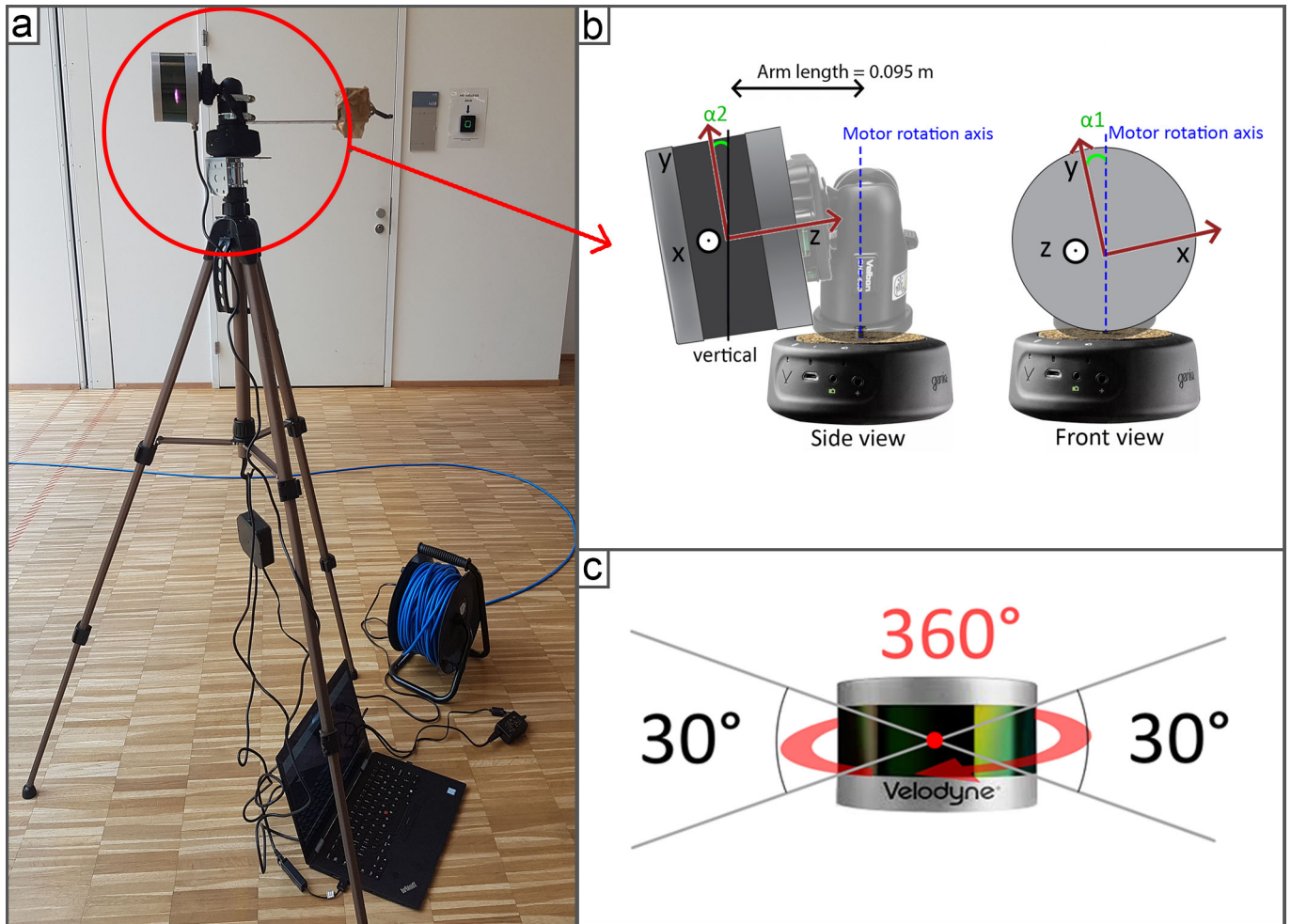
Figure 2. (a) Terrestrial lidar system (TLS); (b) two adjustments angles : collimation axis (α_1) and tilting axis (α_2) between the system and the rotation axis; (c) field of view of the VLP-16

3 Methodology

3.1 Data acquisition operation

Acquisition with our system requires a number of post-processing steps to obtain a scan that correctly represents the scene. For each acquisition, a 360-degree rotation is required to reconstruct a dense and accurate point cloud, the reason for this will be clarified in chapter 3.2. In order to ensure that the system does not record the acceleration and deceleration of the motor at the beginning and end of the rotation, the scans are made for a rotation of more than 360-degrees, which allows a better synchronization with the VLP-16. Once the engine starts its rotation, the scan is then started. The post-processing of the data consists in using the set of points (hereafter frame) produced after each rotation of the laser (10 rotations per second) and applying to it a transformation in relation to the motor speed. Figure 3 takes the example of a teapot to illustrate densification process, with 5 steps described below:

1. Frame at time $t = t_0$: Only a part of the teapot is scanned, corresponding to the lidar field of view (30 degrees). This first frame is used as reference to align the others.

2. Scan at time $t = t_1$: a second part of the teapot is scanned.

3. Representation of the scene when both frames are visible simultaneously. It is necessary to apply a transformation to correctly align both frames. This transformation is equal to a rotation on the y axis in clockwise direction by an angle corresponding to the rotation of the motor between t_0 and t_1.

4. Reconstructed scene after transformation: both frames are now aligned. Frames are incrementally assembled to construct the entire scene.

5. Visualization of the assemblage of frames acquired between time t_0 and t_f.

Assuming a constant geometry of the system, we use a rigid transformation between each frame. This geometrical transformation is characterized by a 4 x 4 matrix

$$T = \begin{bmatrix} a & b & c & 0 \\ d & e & f & 0 \\ g & h & i & 0 \\ j & k & l & 1 \end{bmatrix},$$

with:

– abc, the rotation applied on the x-axis

– def the rotation applied on the y-axis,
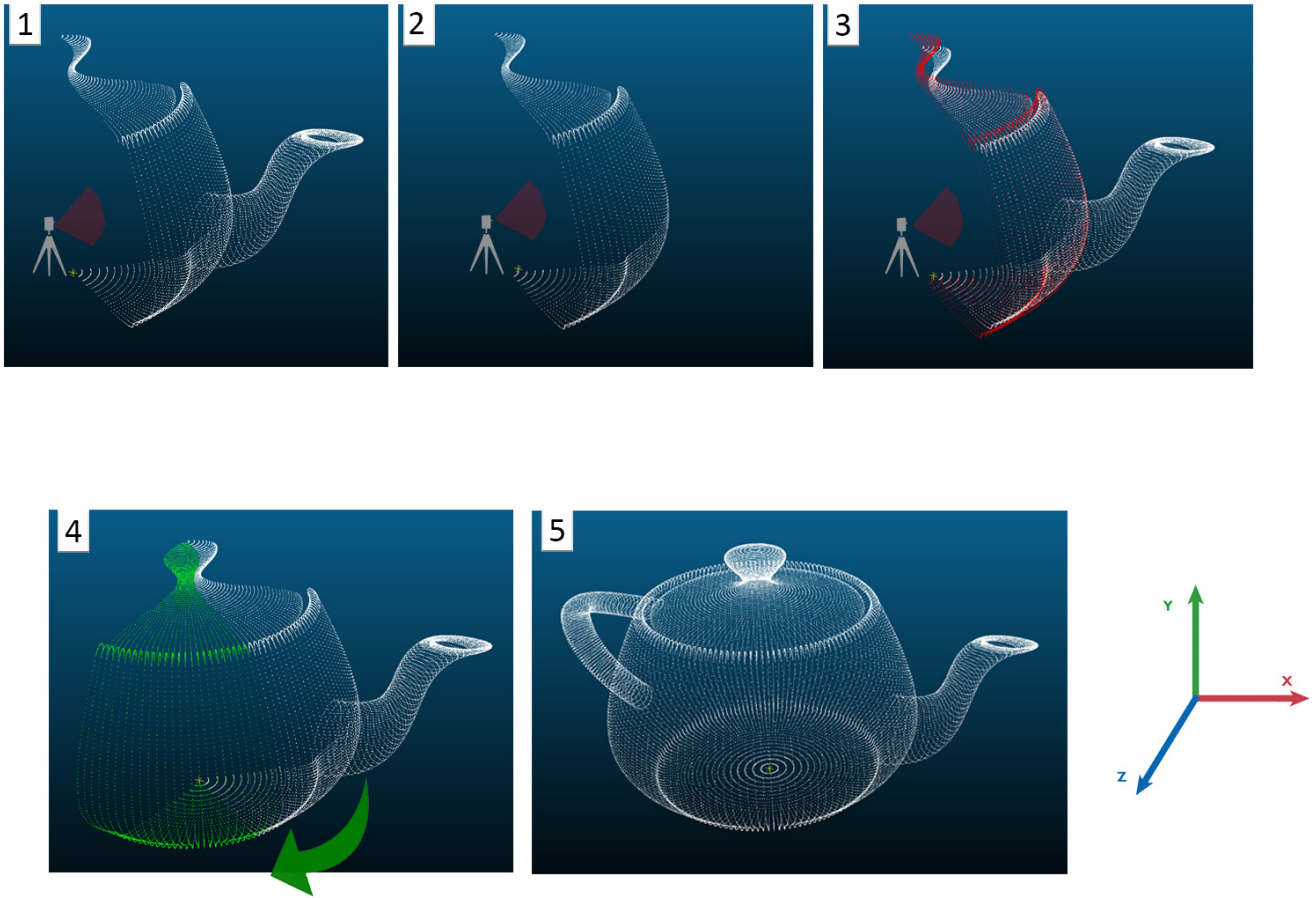
Figure 3. Steps to align the final. This is synthetic example assuming that the lidar is located in the center of the teapot point cloud

- – ghi the rotation applied on the z axis.

- – jkl the translation applied on x, y and z.

In our case, the rotation is applied around the y-axis, the transformation matrix that aligns each frame is equal to:

$$T_1 = \begin{bmatrix} (cos(\beta) & 0 & sin(\beta) & 0 \\ 0 & 1 & 0 & 0 \\ -sin(\beta) & 0 & cos(\beta) & 0 \\ 0 & 0 & 0 & 1 \end{bmatrix},$$

105   with β the angle of the motor, which depends on the time since the start of the scan and the rotation speed. Once all frames are assembled, the entire point cloud can be visualized.

As the VLP-16 Puck has the particularity of being able to scan continuously and at 360-degrees, two sets of symmetrical point clouds representing respectively the points with positive and negative coordinates on the x-axis of the lidar reference frame (see Figure 5a) are created, which are theoretically superposed. This observation is a crucial point of the study as it allows the adjustment of the system in order to maximize this superposition (the adjustment procedure is described in section 3.2).

3.2   Post-processing and data adjustment

Since our system is custom-assembled, there is little control on exact mounting angles, which therefore require adjustments. Thus far, we have supposed that the system is turning around a fixed point corresponding to its optical center. In fact, given that the lidar is positioned on a ball head and a L-shaped piece, it is shifted from the rotation axis. This distance was measured using an electronic caliper and is equal to 0.095 m, for each frame a translation on the z axis was applied. The affine transformation is a matrix presented as follows:

$$T_2 = \begin{bmatrix} 1 & 0 & 0 & 0 \\ 0 & 1 & 0 & 0 \\ 0 & 0 & 1 & 0 \\ 0 & 0 & 0.095 & 1 \end{bmatrix}$$

Another important consideration is the correction to minimize systematic errors. Figure 2b shows two major adjustment parameters described in Neitzel 2006: α_1 for the collimation axis adjustment and α_2 for the tilting axis adjustment. . The manual adjustment of those two systems involves an offset that highly influence the point cloud geometry if uncorrected. As these offsets cannot be measured manually, an automatic adjustment is performed in post-processing.

To determine α_1 and α_2, the Nelder-Mead optimization algorithm is used, which is based on minimizing a continuous function using a simplex of dimensions equivalent to the number of parameters (Lagarias et al., 1998). At each iteration, a point located near the initial simplex is generated involving a new sample if a minimum is found, until convergence.

The resolution of the densified scan is not regular. Indeed the point cloud resolution is very high near the lidar scanner and decreases away from the sensor. Because the algorithms for measuring the distance between two sets of point clouds require a lot of computer resources and must be repeated at each iteration of the Nelder-Mead optimization, the scans are downsampled using a grid average method to an uniform resolution. In addition, the optimization is carried out only for points within the distance range in the best accuracy range of 3 to 7 meters (Glennie et al., 2016).

The optimization seeks to obtain the α_1 and α_2 angles that minimize two functions:

1. During the rotation of the motor, the entire scene is recreated for each of the 16 scan lines. These identical scans are then put back together to form a dense point cloud. The overlap of the scans is influenced by changing the angle α_1 . Thus, the function to optimize corresponds to minimizing the average distance between the 16 full scenes that are superimposed.

2. The second function determines the angle α_2 based on the observation that both sets of symmetrical point clouds produced during the rotation must be exactly superposed. The variation of the angle α_2 creates a doming effect that tends to increase the average distance between both symmetrical point clouds (Figure 5a). α_2 is determined by minimizing this distance.

3.3 Effect of the adjustments and performance of the system

Visually, a wrong adjustment of α_1 results in blur around the scanned scene. A wrong adjustment of the α_2 angle results in a doming effect that increases away from the center. To illustrate this, several scans were carried out in a building of the University of Lausanne. A corridor of dimension 23 by 1.5 meters was scanned and a plane was fitted on the floor surface, which is supposed to be horizontal. This plane is based on a distance interval to the lidar equivalent to the best accuracy range, i.e. between 3 and 7 meters depending on the lidar performance tests (Glennie et al., 2016). This avoids the influence of points too close or too far away, which can distort the theoretical equation of the plane. In addition, the points selected for fitting the plane come from an adequate sub-sampling of the initial scan in order to standardize the density of points over the distance interval. Then, the distance of all points to this theoretical plane is evaluated, which gives an indication of the distribution of errors. Evaluation of the error as a function of the scanning distance was also measured.

Finally, reproducibility tests were performed to evaluate the stability of the system. To this end, the same scene was scanned 8 times in a row. The α_1 and α_2 parameters were then estimated separately. As the system is not transported or disassembled between measurements, the aim of this test was to evaluate the stability of these parameters. The average distance between each of the 8 scans is also evaluated using the M3C2 plugin of Cloudcompare with its default settings, which allows to compute signed (and robust) distances directly between two point clouds.

3.4 Testing the system in different environments

The system has been tested in various environments. For all scans performed, the Syrp Genie Mini has been configured to rotate 360-degrees in 6 minutes. These parameters allowed the acquisition of high point resolution to maximize the information collected while maintaining a reasonable scan time. With this setting, about 10 millions points per scan are collected. The first tests were carried out in a building of the University of Lausanne is characterized by vast surfaces and volumes. Then, the system was then used in a confined environment with no available GNSS signal: the Baulmes mines, a limestone mine disaffected at the end of the Second World War.

In these environments, several scans were assembled using the iterative closest point (ICP) alignment algorithm (Besl, P. J., McKay in 1992). This is the most popular method alignment approach for point clouds, which searches for nearest neighbors to minimize the distance between two point clouds.

3.5 Comparison with a high-cost system and field measurements

Our low-cost terrestrial lidar system was then compared to two other systems that fall into the high-cost category. These lidar systems are the Ilris 3D Optec and the Geoslam ZEB-REVO (table 3). The tests were carried out indoors and included one

measurement for each system. First, Figure 5 displays a picture of the scanned scene. As shown, objects were placed on the scene so that validation measurements could be taken with a tape measure in addition to the width and length of the corridor and the height of the ceiling. These distances were then measured for the scans coming from all three terrestrial lidar systems and

170   compared to the measurements taken by hand. The different scans were also superimposed with an ICP algorithm to evaluate the average distance between the point clouds.
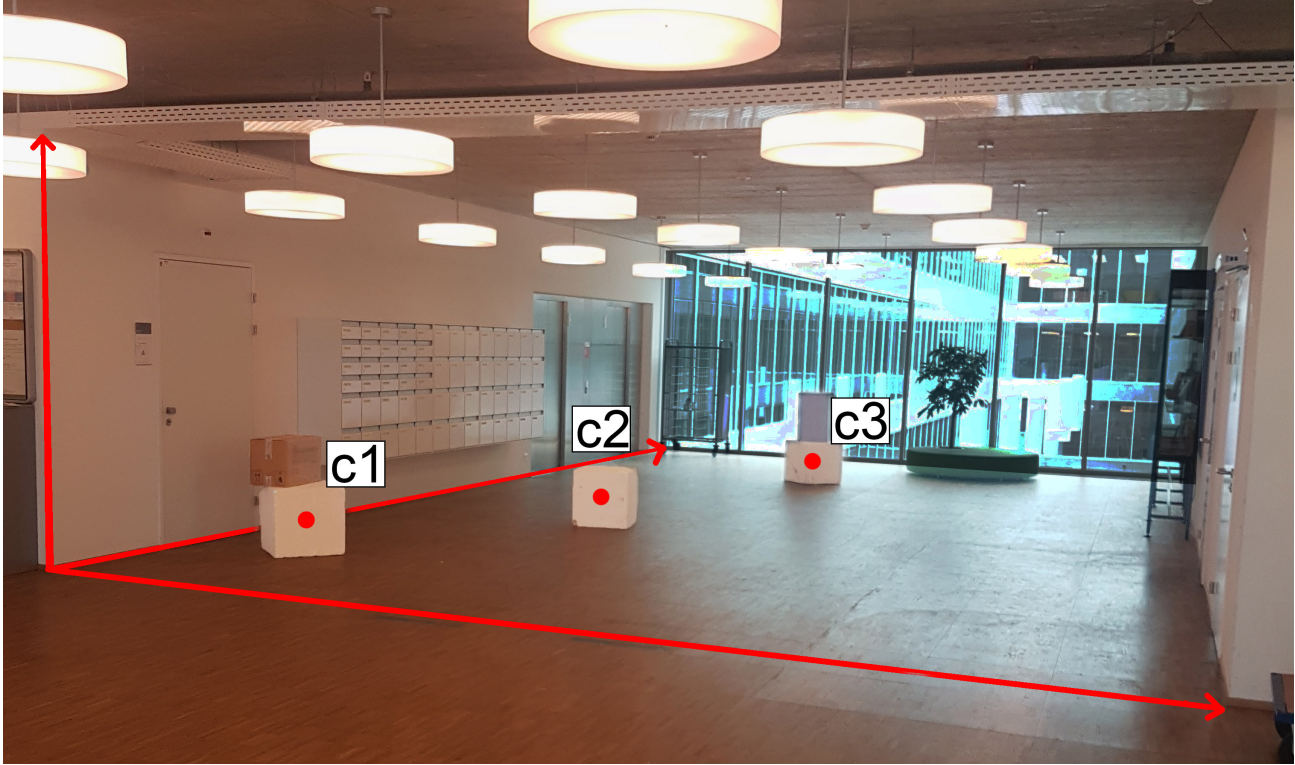
Figure 4. Picture of the scanned scene for lidar and distances comparison

Table 3. Main characteristics of lidar used

Parameter	Ilris-3D	Geoslam ZEB-REVO
Range	1200 m	30 m
Field of view	40 x 40 degrees	270 x 360-degrees
Ranging accuracy	7 mm @ 100 m	1 - 3 cm
Laser wavelength	1535 nm	905 nm
laser acquisition rate	2500 - 3500 points/sec	43.200 points/sec

4 Results

All point clouds are visualized in the CloudCompare software. An EDL (Eye Dome lighting) shading filter allowing the creation of real-time shading has been applied for better visualization (CloudCompare, 2019).

 4.1   Effects of adjustments
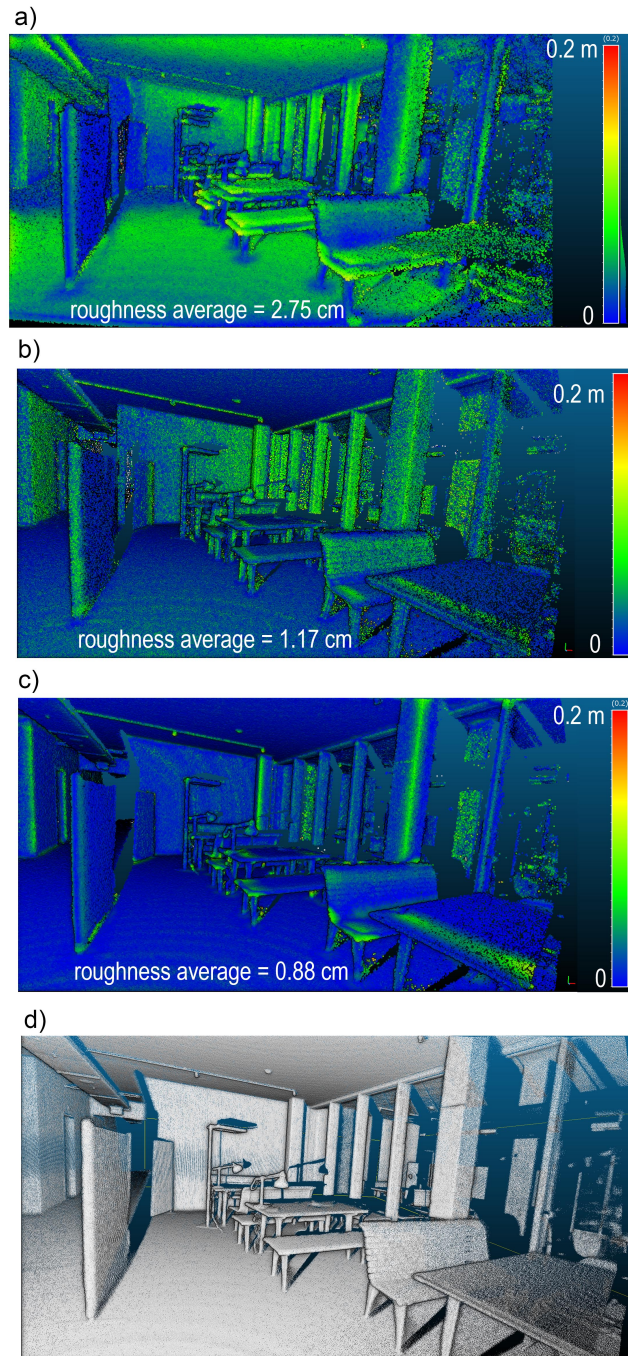
Figure 5. Point cloud roughness for adjustment steps : (a) Scan without adjustments; (b) Scan after adjustments of α_1 and α_2, ; (c) final scan; (d) final scan (EDL filter)

Figure 5 shows the result of a scan that was carried out indoors in a work area of the University of Lausanne. Figure 5a shows the scene after the alignment of the different frames produced by the VLP-16 during the scan. A kind of blur caused by the splitting of the scene is observed. No processing has yet been applied, so the parameters α_1 and α_2 are set to 0. The color scale represents the roughness of the point cloud (for a radius of 0.2 m). Figure 5b shows the scene after adjusting the α_1 and α_2 parameters. The average roughness is equal to 1.17 cm. Figure 5c shows the scene where only the scanned points corresponding to the positive coordinates on the x-axis are displayed (i.e., 50% of the data are discarded). In addition, a sub-sampling at 0.005m is applied using a grid average method and a statistical outlier removal is performed in cloudCompare. The average roughness is equal to 0.88 cm. Figure 5d is a copy of 5c with an Eye-dome-lighting filter.

Figure 6 shows the error corresponding to the distance of the points from the theoretical plane and the error histogram for the three adjustments steps respectively.
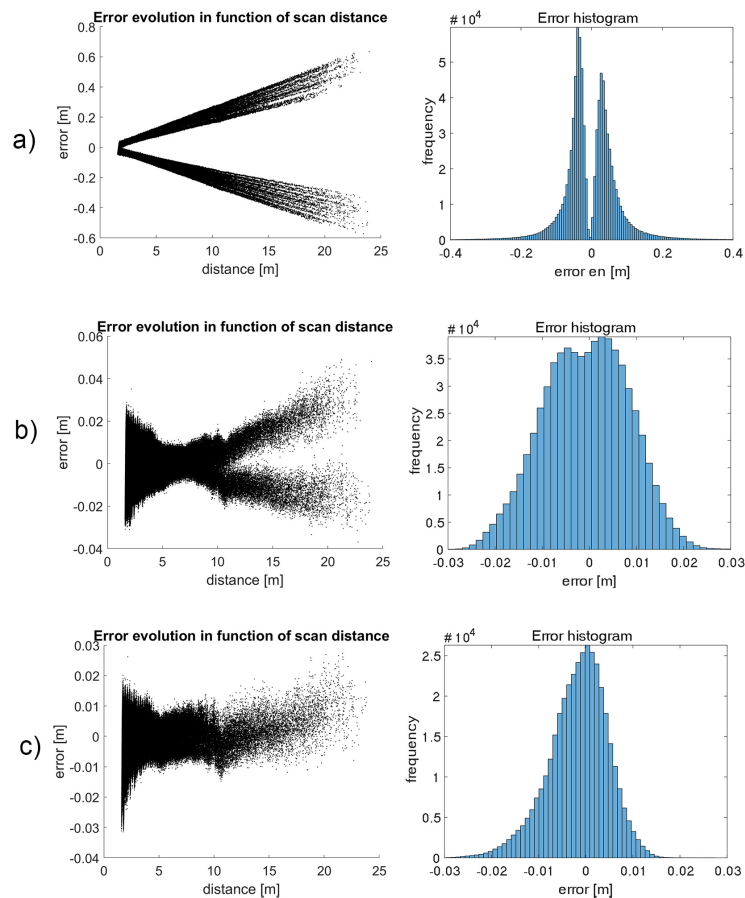
Figure 6. Effects of adjustments in relation to a theoretical plane : (a) Error estimation before calibration; (b) Error estimation after adjustments; (c) Error estimation after post-treatment

4.2 Overview of the densification quality

Figure 7a provides an overview of a scan performed indoors after adjustments. A photograph of the scanned scene with the same viewing angle is shown in Figure 7b. Note the improvement compared to Figure 1 where the VLP-16 was used alone.

Figures 8a and 8b show two previews of scans performed at the Baulmes mines.

190   Figure 8c shows the result of the registration of 4 point clouds in the Baulmes mines. The points corresponding to each of the acquisitions are represented in a different color to highlight the registration. It should be noted that the clouds have not been cleaned to removed outliers, so we can see that the sensor has scanned itself. The results are characterized by a spacing set at 0.005 meters and is visually realistic.

a)

b)
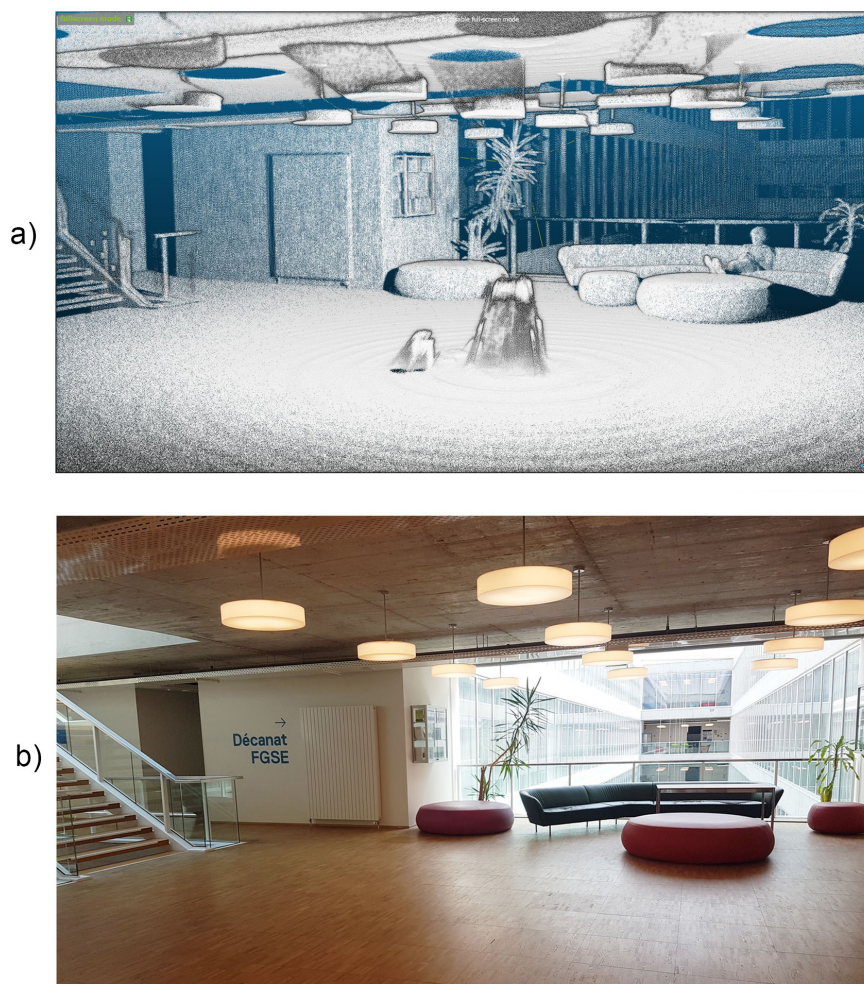
Figure 7. Example of point cloud densification after adjustments of the system : (a) Result of an indoor point cloud densification; (b) Picture of the scene
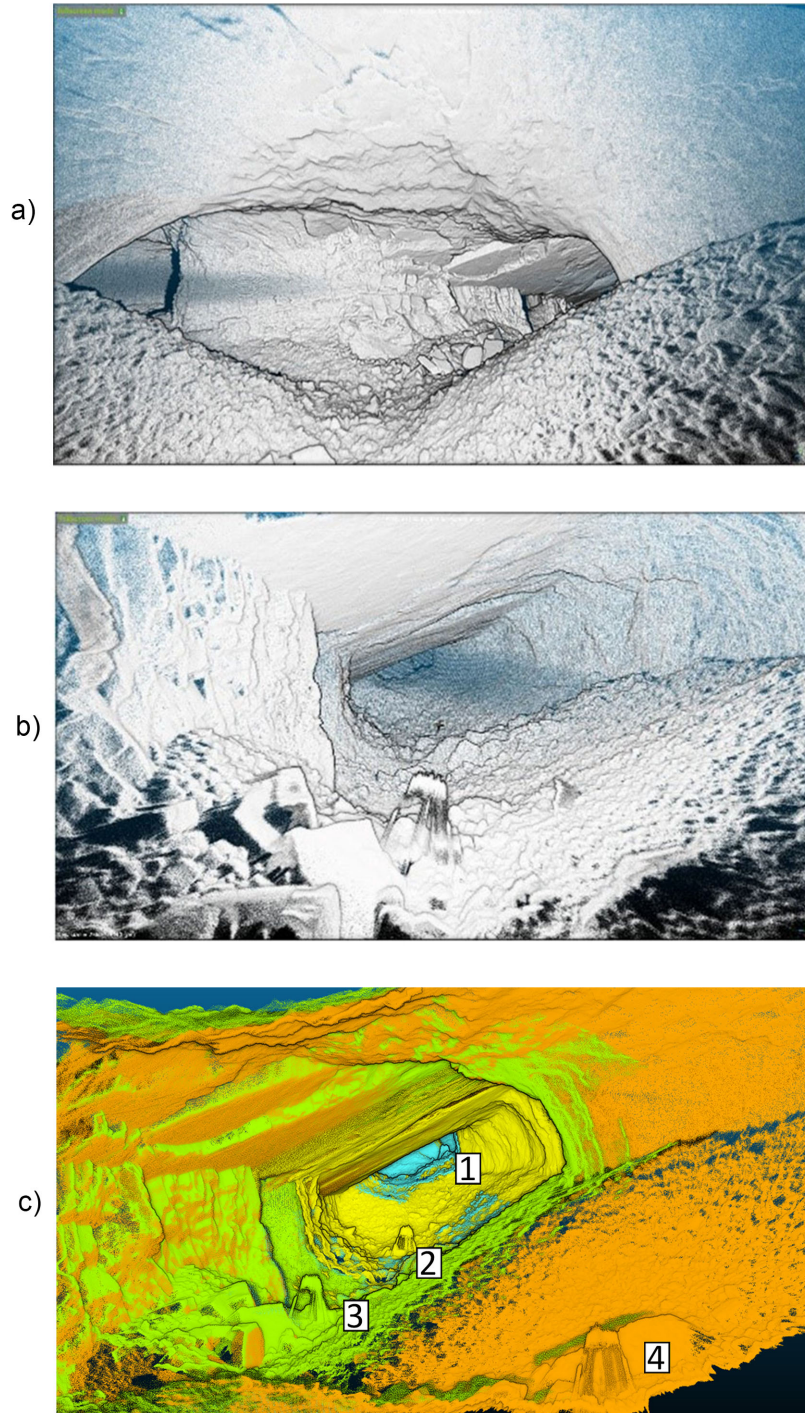
Figure 8. Scanned scenes in Baulmes mines. The height of the gallery is about 3.5 m : (a) Mine example 1; (b) Mine example 2; (c) Point cloud registration in the mine

4.3 Data analysis and validation

195   During the visualization of the point clouds, we observed the presence of an artifact on all of our measurements. Figure 9 illustrates this artifact, which is characterized by wavelets near the system that fade away with distance.
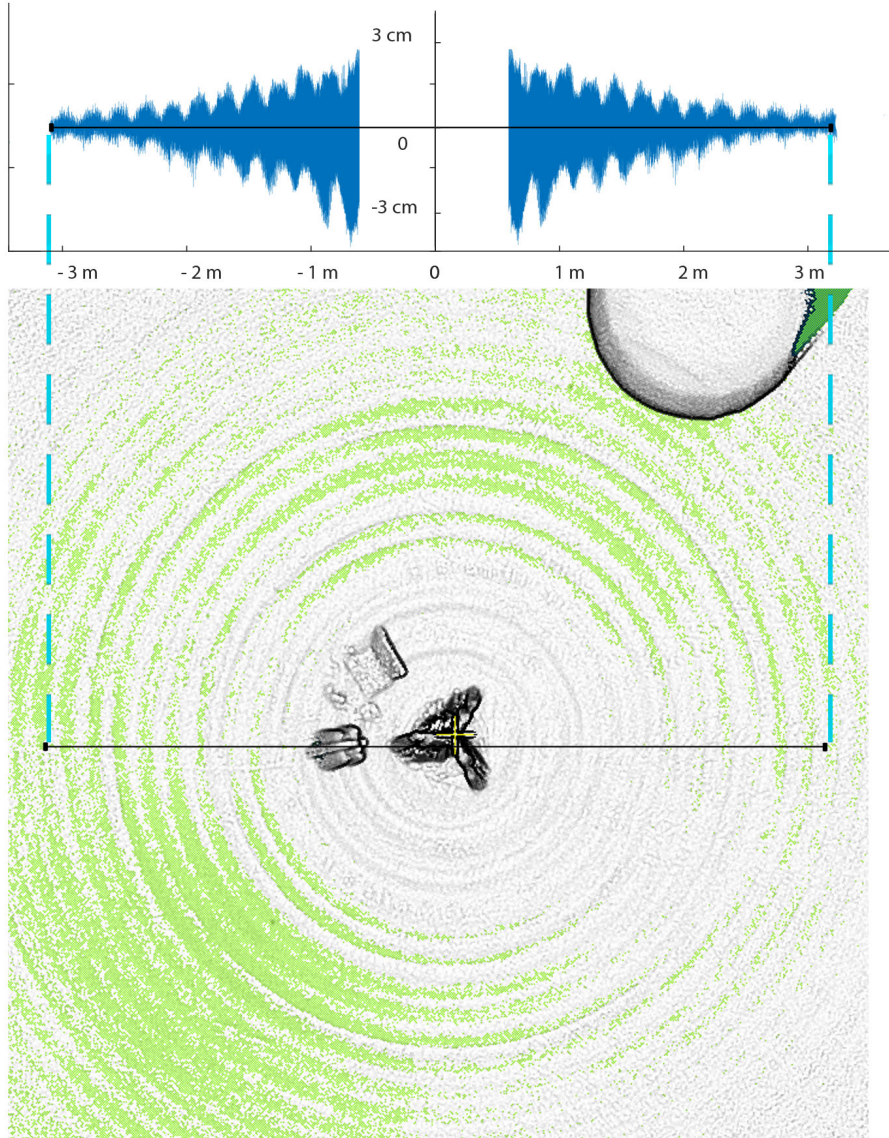
Figure 9. Artifact present near the TLS and its corresponding amplitude

Table 4 shows the ability of the system to reproduce the same point cloud by comparing 8 consecutive measurements. Each of these measurements is compared to the other 7 by measuring the average distance between pairs of scans (in meters). Table 5 shows the variation of the parameters α_1 and α_2 during this reproducibility test. Table 6 summarizes the different measurements made with the VLP-16, Ilris-3D and Geoslam. The data are also compared with manual measurements.

Table 4. Distance between all of the 8 scans of the reproductibility test

Scan number	1	2	3	4	5	6	7	8
1	0.000	0.014	0.019	0.018	0.020	0.021	0.022	0.016
2		0.000	0.019	0.019	0.020	0.022	0.021	0.016
3			0.000	0.013	0.015	0.016	0.016	0.019
4				0.000	0.014	0.016	0.016	0.019
5					0.000	0.015	0.015	0.020
6						0.000	0.015	0.022
7							0.000	0.021
8								0.000

Table 5. Variability of α_1 and α_2 parameters during reproducibility test

Num.	α_1 [degre]	α_2 [degre]
1	0.40	-0.00
2	0.40	-0.01
3	0.09	-0.03
4	0.11	-0.04
5	0.05	0.00
6	0.05	0.00
7	0.07	0.02
8	0.34	-0.09

Table 6. Comparison of field and lidar measurements

	Field [m]	VLP [m]	Ilris [m]	Geoslam [m]
Ceiling	3.005	3.001	3.003	2.964
Length	11.945	11.932	11.970	11.931
Width	7.145	7.127	7.117	7.087
Cube dimension	0.500	0.500	0.498	0.509
c1 -c2	2.715	2.730	2.719	2.741
c2 - c3	4.635	4.645	4.625	4.832
c1 - c3	7.545	7.519	7.478	7.473
ABS Mean difference	Field [m]	0	0.0123	0.0197	0.0596

To validate the registration, the comparison of the distances between the points coming from our assembly and those coming from GeoSLAM was carried out using CloudCompare with the option "Cloud to cloud distance". The average distance between both point clouds and the standard deviations of these distances are shown in Table 4.

Table 7. Mean distance between Ilris, Geoslam and Velodyne TLS (M3C2 distance)

	Mean distance [m]
Optec Ilris vs. VLP-16 TLS	$\pm$ 0.025
Optec Ilris vs. Geoslam	$\pm$ 0.067
VLP-16 TLS vs Geoslam	$\pm$ 0.051

5   Discussion

5.1   Data analysis before and after adjustment

As shown in Figure 5, adjustment is a fundamental step in producing accurate 3D modeling of an environment.

The use of the two symmetrical datasets produced during an acquisition using the VLP-16 is a key element in the optimization of the system. However, as shown in Figure 5b, the roughness calculation tells us that the entire point cloud could silll be smoother. For this reason, we decided to keep only half of the points (Figure 5c and Figure 5d) in order to obtain a sharper representation of the scene. This choice will be justified after the analysis of the following analysis.

The error depends on the distance to the lidar. Before adjustment, the distance to the theoretical plane varies from about $\pm$ 4 cm ($\mu \pm 1\ \sigma$) for the closest points to the lidar to 59 cm ($\mu \pm 1\ \sigma$) for a scan distance of 23 m (Figure 6a). After adjustment of parameters α_1 and α_2, the entire point cloud approaches the theoretical surface, as shown in Figure 6b. However the evolution

of the error as a function of distance is still not constant and tends to increase linearly with the scan distance. The minimum error is logically in the point range where the theoretical plane is situated. The bimodal error histogram shown in Figure 6b and (centered at $\pm$ 0.5 cm) shows that the superposition between the two halves of the scan is still not entirely accurate despite the adjustment performed.

The evolution of the error as a function of the scanning distance when keeping only one half of the scan (Figure 6c) shows an accuracy range of $\pm$ 2.5 cm ($\mu \pm 1.5\ \sigma$), which remains within the accuracy range given by Velodyne. The post-processing steps and the adjustment of mounting angles has allowed to drastically reduce errors; however, the adjustment parameters vary greatly between scans, as shown in table 5 and table 6. This can be explained by the assembly of our lidar system being relatively unstable. The impact of the adjustment, and particularly the need to repeat the adjustment for each scan, could be alleviated by welding together the different components of the system.

5.2 Performance and stability of the TLS

According to the manufacturer's website, the VLP-16 Puck allows data acquisition at a distance of 100 m for an accuracy of $\pm$ 3 cm, under optimal acquisition conditions. Various stability tests have been carried out in a metrology laboratory, which indicates an accuracy of $\pm$ 2 cm for an acquisition distance of 5 meters to a white and flat target (Glennie, et al., 2016).

Reproducibility tests tell us that the system is quite stable when it is not moved or disassembled. The α_1 adjustment parameter shows a slight variation for scans 1, 2 and 8. This can be explained by the Nelder-Mead algorithm which finds a local and not a global minimum of the function.

The calculation of the average distance between all scans (table 4) indicates a small variation in the scanned scene. The measured distances are mostly below 2 cm, confirming the tests performed by Glennie, et al. 2016 and may be related to noise. We can see a correlation between scan pairs having similar adjustment parameters (scans 1, 2, 8) and their average distances.

5.3 Comparison with high-cost hardware and field measurements

The measurements taken manually in the field have enabled comparisons with the scans obtained with our system. Table 6 shows that the measurements taken with the VLP-16 TLS are closest to ground truth, with an average of 1.23 cm compared to 1.97 cm for the Optec and 5.96 cm for the Geoslam. This result should be taken with caution as it may be specific to our experimental setup. It should also be taken into account that a sub-sampling at 0.5 cm from the scans was performed using a grid average method.

After alignment using an ICP algorithm, the scans could be compared and are presented in Table 7. Assuming that the Optec system is the most accurate, our system achieves a good performance with an average distance of $\pm$ 2.5 cm. Geoslam obtains a lower level of accuracy with an average of $\pm$ 6.7 cm.

5.4 Origin of the short-range artifacts

Visually, this artifact is easily observed in the results of scans near the tripod,when data acquired on a flat surface. Figure 9
245   shows the influence of this artifact on the scan. We notice that the error spreads in the form of regular waves and fades away as it moves away from the lidar. It has a magnitude of 3 cm at the closest to the lidar and drops below 1.5 cm at a distance of 3 m. The wave frequency is about 20 cm. A hypothesis on the origin of this artifact would be related to the length of the arm which was measured manually. It turns out that errors in the length of the arm has no influence on the occurrence of these artifacts, but instead creates horizontal deformations. We also tested by using each laser separately, by using another tripod, and by varying
250   the parameters and changing the motor speed. However, the artifacts remain constant (same distance and amplitude between waves). This indicates that the artifacts seem to be related to the lidar itself. Since the error appears to be regular, it would be conceivable to correct outliers by modifying each point according to the distance to the lidar.

6 Conclusion

This paper presents a low-cost terrestrial lidar system based on the use of a Velodyne VLP-16. Comparisons with high-precision
255   models allow validating the accuracy of the system, which seems promising. As shown in the results, our system requires adjustment for each scan performed. These adjustments are made in post-processing and are possible thanks to the data acquisition geometry of the VLP-16. This could be avoided if the system components were welded together. However, we wanted to keep the possibility separating these elements in order to use the lidar for other projects, for example. The use of the lidar system in an underground mine demonstrates the potential applications of such a system in particular in the field of geosciences.

260   *Code availability.* Velodyne TLS

    GitHUB repository

Data availability.

Code and data availability.

Sample availability.

265   *Video supplement.*

Baulmes

Reclere

Milandre

Rolex Learning Center

270 **Appendix A**

A1

Author contributions. JB developed the methodology, carried out the field experiments and wrote the manuscript, MHD provided advice and methodological guidance and contributed to the manuscript, GM proposed the initial framework, provided supervision and contributed to the manuscript

275 *Competing interests.*

Disclaimer.

Acknowledgements. We thank Stephane Affolter, Pierre-Xavier Meury and Eric Gigandet for access to caves for testing our method

References

Amiri Parian, J. and Grün, A.: Integrated laser scanner and intensity image calibration and accuracy assessment, in International Archives of the Photogrammetry, Remote Sensing and Spatial Information Sciences, vol. 36, pp. 18–23, ISPRS., 2005.

Besl, P. J. and McKay, N. D.: Method for registration of 3-D shapes, in Sensor Fusion IV: Control Paradigms and Data Structures, vol. 1611, pp. 586–606, International Society for Optics and Photonics., 1992.

Brideau, M.-A., Sturzenegger, M., Stead, D., Jaboyedoff, M., Lawrence, M., Roberts, N. J., Ward, B. C., Millard, T. H. and Clague, J. J.: Stability analysis of the 2007 Chehalis lake landslide based on long-range terrestrial photogrammetry and airborne LiDAR data, Landslides, 9(1), 75–91, doi:10.1007/s10346-011-0286-4, 2012.

Dewez, T. J. B., Yart, S., Thuon, Y., Pannet, P. and Plat, E.: Towards cavity-collapse hazard maps with Zeb-Revo handheld laser scanner point clouds, The Photogrammetric Record, 32(160), 354–376, doi:10.1111/phor.12223, 2017.

Glennie, C. and Lichti, D. D. (2010). Static Calibration and Analysis of the Velodyne HDL-64E S2 for High Accuracy Mobile Scanning, Remote Sensing, 2(6), 1610–1624, doi:10.3390/rs2061610, 2010.

Glennie, C. and Lichti, D. D.: Static Calibration and Analysis of the Velodyne HDL-64E S2 for High Accuracy Mobile Scanning, Remote Sensing, 2(6), 1610–1624, doi:10.3390/rs2061610, 2010.

Glennie, C. L., Kusari, A. and Facchin, A.: Calibration and stability analysis of the VLP-16 laser scanner, Int. Arch. Photogramm. Remote Sens. Spatial Inf. Sci., XL-3/W4, 55–60, doi:10.5194/isprs-archives-XL-3-W4-55-2016, 2016.

Jaboyedoff, M., Oppikofer, T., Abellán, A., Derron, M.-H., Loye, A., Metzger, R. and Pedrazzini, A.: Use of LIDAR in landslide investigations: a review, Nat Hazards, 61(1), 5–28, doi:10.1007/s11069-010-9634-2, 2012.

James, M. R. and Quinton, J. N.: Ultra-rapid topographic surveying for complex environments: the hand-held mobile laser scanner (HMLS): ULTRA-RAPID TOPOGRAPHIC SURVEYING: THE HMLS, Earth Surf. Process. Landforms, 39(1), 138–142, doi:10.1002/esp.3489, 2014.

Kersten, Thomas Sternberg, Harald Mechelke, Klaus. (2005). Investigations into the accuracy behaviour of the terrestrial laser scanning system Mensi GS100. Optical 3-D Measurement Techniques VII. 1. 122-131.

Lagarias, J. C., Reeds, J. A., Wright, M. H. and Wright, P. E.: Convergence Properties of the Nelder–Mead Simplex Method in Low Dimensions, SIAM J. Optim., 9(1), 112–147, doi:10.1137/S1052623496303470, 1998.

Laurent, A., Moret, P., Fabre, J. M., Calastrenc, C., Poirier, N.: La cartographie multi-scalaire d'un habitat sur un site accidenté: la Silla del Papa (Espagne), 2019.

Lerma, J. L. and García-San-Miguel, D.: Self-calibration of terrestrial laser scanners: selection of the best geometric additional parameters, ISPRS Ann. Photogramm. Remote Sens. Spatial Inf. Sci., II–5, 219–226, doi:10.5194/isprsannals-II-5-219-2014, 2014.

Li, R., Liu, J., Zhang, L. and Hang, Y.: LIDAR/MEMS IMU integrated navigation (SLAM) method for a small UAV in indoor environments, in 2014 DGON Inertial Sensors and Systems (ISS), pp. 1–15, IEEE, Karlsruhe, Germany., 2014.

Lichti, D. D.: Error modelling, calibration and analysis of an AM–CW terrestrial laser scanner system, ISPRS Journal of Photogrammetry and Remote Sensing, 61(5), 307–324, doi:10.1016/j.isprsjprs.2006.10.004, 2007.

Lichti, D., Brustle, S., Franke, J. (2007). Self-calibration and analysis of the Surphaser 25HS 3D scanner. Proceedings of the Strategic Integration of Surveying Services, FIG Working Week, Hong

Lim, M., Petley, D. N., Rosser, N. J., Allison, R. J., Long, A. J. and Pybus, D.: Combined Digital Photogrammetry and Time-of-Flight Laser Scanning for Monitoring Cliff Evolution, The Photogrammetric Record, 20(110), 109–129, doi:10.1111/j.1477-9730.2005.00315.x, 2005.

315 Michoud, C., Carrea, D., Costa, S., Derron, M.-H., Jaboyedoff, M., Delacourt, C., Maquaire, O., Letortu, P. and Davidson, R.: Landslide detection and monitoring capability of boat-based mobile laser scanning along Dieppe coastal cliffs, Normandy, Landslides, 12(2), 403–418, doi:10.1007/s10346-014-0542-5, 2015.

Neitzel, F. (2006). Investigation of Axes Errors of Terrestrial Laser Scanners.

Northend, C. A., Honey, R. C. and Evans, W. E.: Laser Radar (Lidar) for Meteorological Observations, Review of Scientific Instruments,
320 37(4), 393–400, doi:10.1063/1.1720199, 1966.

Royán, M. J., Abellán, A., Jaboyedoff, M., Vilaplana, J. M. and Calvet, J.: Spatio-temporal analysis of rockfall pre-failure deformation using Terrestrial LiDAR, Landslides, 11(4), 697–709, doi:10.1007/s10346-013-0442-0, 2014.

Royán, M. J., Abellán, A., Jaboyedoff, M., Vilaplana, J. M. and Calvet, J.: Spatio-temporal analysis of rockfall pre-failure deformation using Terrestrial LiDAR, Landslides, 11(4), 697–709, doi:10.1007/s10346-013-0442-0, 2014.

325 Teza, G., Galgaro, A., Zaltron, N. and Genevois, R.: Terrestrial laser scanner to detect landslide displacement fields: a new approach, International Journal of Remote Sensing, 28(16), 3425–3446, doi:10.1080/01431160601024234, 2007.

Williams, J. G., Rosser, N. J., Hardy, R. J., Brain, M. J. and Afana, A. A.: Optimising 4-D surface change detection: an approach for capturing rockfall magnitude–frequency, Earth Surface Dynamics, 6(1), 101–119, doi:https://doi.org/10.5194/esurf-6-101-2018, 2018.